

The source parameters of earthquakes of Bishkek geodynamic proving ground (Northern Tien Shan)

Naylya Sycheva *

Science Research Station of the RAS in Bishkek city, Kyrgyzstan

Abstract. Based on the method of polarity of signs of P -waves, the focal mechanisms of 1674 earthquakes with $M \geq 1.6$, which occurred on the territory of the Bishkek geodynamic proving ground (BGPG) from 1994 to 2020, were determined. Some characteristics of the complete catalogue are presented. Quantitative distributions by the type of mechanisms and diagrams of azimuths of the main stress axes are constructed. A variety of focal mechanism of earthquake is observed, most of them are reverse fault, oblique reverse fault, and horizontal strike-slip fault. The compression axis for most of the events has a north-northwest direction and a sub-horizontal position. For 183, dynamic parameters (DP, source parameters) were obtained: spectral density Ω_0 , corner frequency f_0 , scalar seismic moment M_0 , source radius (Brune radius) r , and stress drop $\Delta\sigma$. The correlations between DP and energy characteristic (magnitude) and scalar seismic moment are investigated. The smallest correlation coefficient was obtained for stress drop.

Introduction

The Kyrgyz seismological network, installed in 1991 on the territory of the Northern Tien Shan, consists of 10 digital, broadband stations, each of which is equipped with an STS-2 sensor (Fig. 1).

It was found that the stations of the KNET network are low-noise [1] and site under stations does not generate resonance effects [2]. The catalogue of earthquakes created on the basis of the KNET network database is representative [3], which makes it possible to carry out various seismological studies on its basis.

The propagation of seismic waves in rocks is a complex process characterized by a number of parameters. It is conventionally accepted to divide the parameters into kinematic and dynamic. On the basis of seismic waves, various source parameters of earthquakes are calculated, which are also usually divided into kinematic and dynamic ones.

The focal mechanism is a geomechanical model of an earthquake source based on instrumental data from seismic records. The source model, presented in three-dimensional form, characterizes the orientation of the axes of the main relieved stresses and the position of the nodal planes of displacement along the rupture in the seismic source and is indirectly

* Corresponding author: ivtran@mail.ru

related to tectonic stresses. The focal mechanism refers to the kinematic characteristic of the source.

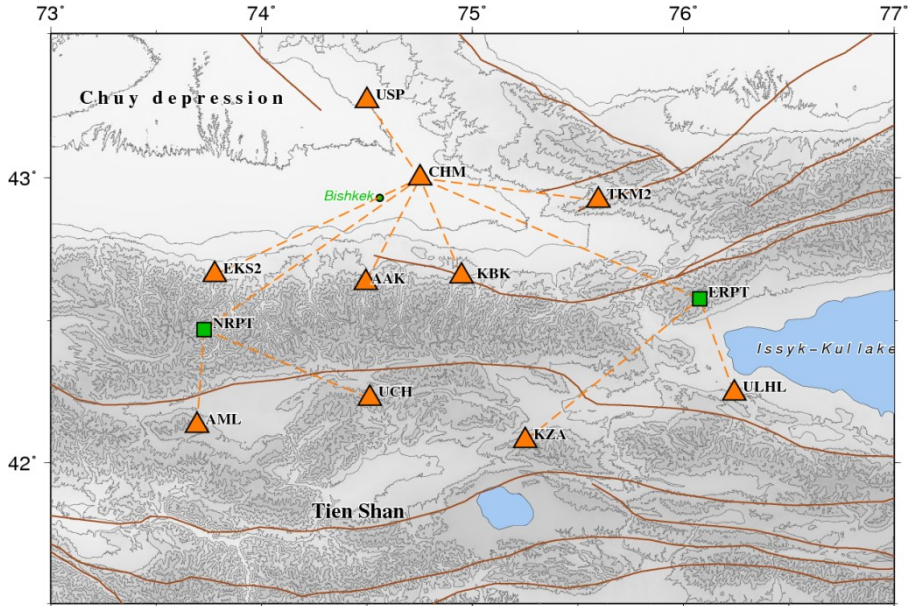


Fig. 1. Position of KNET network stations (triangles) and repeaters (squares).

The dynamic characteristics of seismic waves make it possible to determine such source parameters of earthquakes as the source radius r , scalar seismic moment M_0 , stress drop $\Delta\sigma$ etc., which are related to dynamic parameters.

The purpose of this work is to calculate the source parameters of earthquakes for their further use in determining the stressed-deformed state of the earth's crust of Northern Tien Shan.

Methodology

Focal mechanisms (FM). The overwhelming amount of experimental information accumulated in modern seismology on the mechanisms of earthquake sources was obtained on the basis of data on the polarity of arrivals of seismic waves. At the present time, in the conditions of equipment of an increasing number of seismic stations with digital equipment, this source continues to be the most important [4-6]. When interpreting the picture of the first arrivals, a two-dipole seismic source is considered according to [7]:

$$m_{ij} = (t_i t_j - p_i p_j) / \sqrt{2}, \quad (1)$$

where t , p are unit direction vectors for the tension and compression axes. The nodal surface for P -waves are two mutually perpendicular planes in the considered case of an isotropic elastic medium. As a rule, the focal mechanism is characterized by the orientation in space of its main axes.

One of the conditions for the reliable determination of the focal mechanism from the signs of the arrival of P -waves is the completeness of the surrounding of the epicenter by observation points. In the conditions of the KNET network, for the calculation of the focal mechanism, only those earthquakes that occurred in the territory bounded by the coordinates of the network edge stations can be considered: 42.0–43.0° N. and 73.75–76.0° E, which is a small area of 100 × 300 km² located on the territory of the Northern Tien

Shan (green rectangle in Fig. 2). Potentially, the focal mechanism can be determined for earthquakes marked in black. The earthquakes for which the focal mechanisms were obtained are marked in green. They account for more than 55% of the number of events that occurred in the territory bounded by the green rectangle.

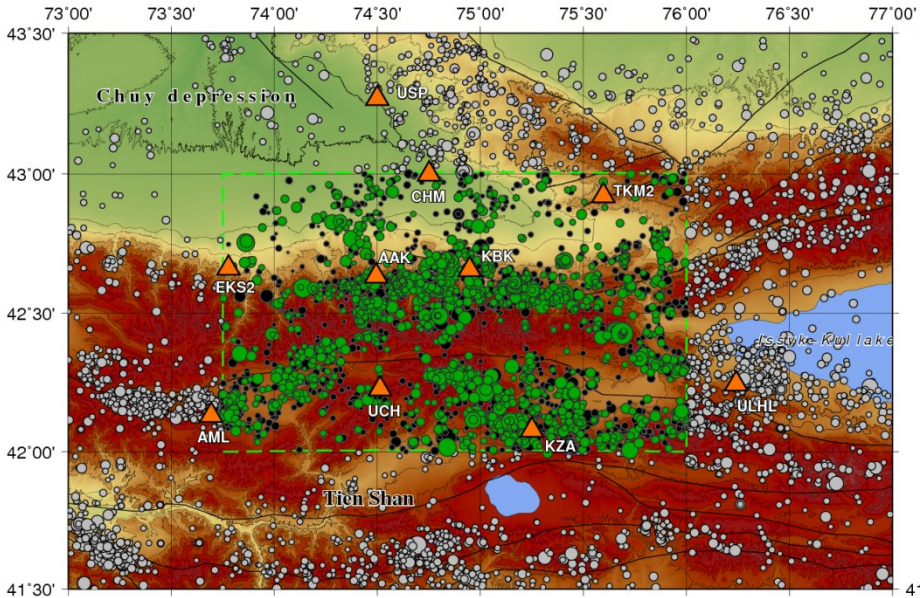


Fig. 2. The earthquakes location of according to the data of the KNET network. The green rectangle (dashed line) is the territory bounded by the coordinates of the edge stations of the KNET network. Earthquakes for which the focal mechanisms are determined by the polarity of arrivals of seismic waves (1674 events) are marked in green.

To calculate the focal mechanisms, the FPFIT program was used [8-12], which finds solutions for a double pair of rupture planes (initial model) that best suit the given set of recorded values of the first arrivals of an earthquake.

Dynamic parameters. To calculate the dynamic parameters, it is necessary to construct a source spectrum and determine its characteristics - spectral density Ω_0 and corner frequency f_0 (time of rupture in the source). The method for calculating the source spectrum in a KNET network is presented in detail in [13-14] and is not considered here. The spectral density Ω_0 is used to determine the scalar seismic moment M_0 . To calculate M_0 the expression [15] is used:

$$M_0 = 4\pi\rho R V_s^3 \Omega_0 / \Psi_0 \quad (2)$$

where R is the distance from the source to the reference point, where the spectrum is determined, ρ is the density of rocks in the source area, Ψ_0 is the directional factor of radiation from the source (for a source described by a displacement jump on the rupture plane), the average value of this factor is taken as 0.64 [16].

The source radius is determined by the formula [17-19]

$$r = k V_s / f_0, \quad (3)$$

where k is a numerical coefficient depending on the source rupture model. The work uses the Brune model [14], for which this coefficient has a value of $k = 0.37$. To calculate the source radius, it is necessary to know the corner frequency, which is determined from the source spectrum and corresponds to the rupture time in the source point.

The value of the stress drop $\Delta\sigma$ characterizes the average difference between the shear stress in the fault before the earthquake, σ_0 , and σ_1 after it, [20]. To calculate the stress drop, the expression [21] is used:

$$\Delta\sigma = 7M_0/16r^3. \tag{4}$$

Seismic energy can be estimated from the spectral parameters Ω_0 and f_0 of seismic waves at a reference point at a distance from the source [22], with the contribution of S -waves being the most significant. Compact expressions for E_S can be obtained if the directivity of radiation from the source is not taken into account [22-23]. A convenient expression relating seismic energy, seismic moment and corner frequency [23]:

$$E_S = \frac{1}{2} \pi^2 \Psi_0^2 M_0^2 f_0^3 / \rho V_S^5 \approx 2M_0^2 f_0^3 / \rho V_S^5. \tag{5}$$

Since the velocity of S -waves is nothing more than $(G/\rho)^{1/2}$, it follows from expression (5) that the given seismic energy is proportional to factor $(f_0/V_S)^3$

$$e_{PR} = 2 \cdot (M_0/G) f_0^3 / V_S^3. \tag{6}$$

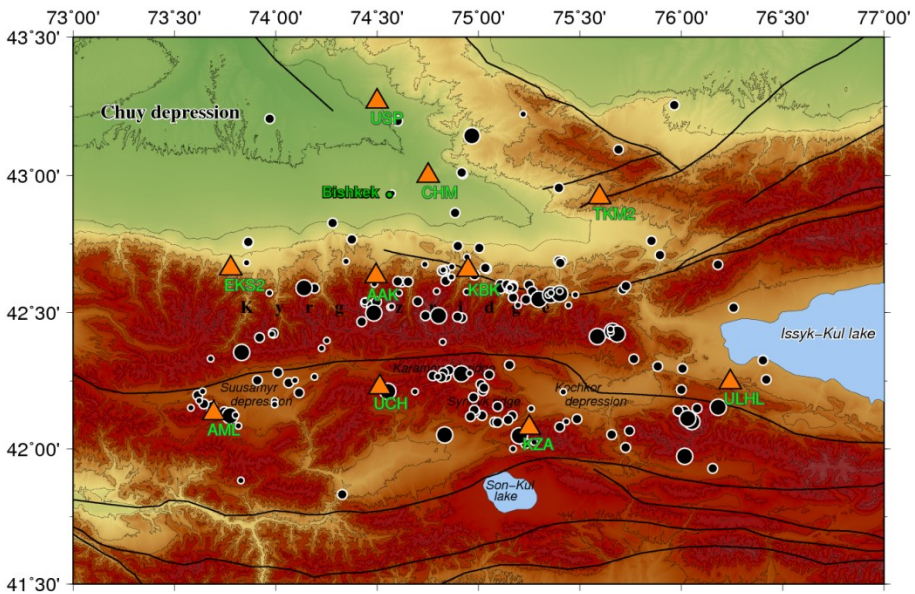


Fig. 3. Earthquakes epicentral location of (183 events). The minimum circle corresponds to the event with $M = 2.7$, the maximum - with $M = 6.0$ Triangles - KNET stations location. Black lines are regional faults.

As the initial data, we used the waveforms of earthquakes that occurred in the territory bounded by the coordinates of the edge stations of the KNET network for 1998–2017 with $K = 8.7 - 14.8$. Geological faults, geographical names of some ridges in the study area and the epicentral location of the seismic events under consideration are shown in Fig. 3. The main part of earthquake epicenters is located on the northern slopes of the Kyrgyz ridge, ridge Karamoynok, mount Sandyk and in the area of the Suusamyr and Kochkor depressions.

Results

Focal mechanisms. As a result of the application of the method for determining the focal mechanisms based on the polarity of the arrival of *P*-waves at the station, the focal mechanisms of 1674 earthquakes were determined and a catalogue was compiled (Fig. 4). The main part of the catalogue of focal mechanisms is made up of weak events ($M = 1.6–2.5$) that occurred at a depth of 5–15 km. Most of the earthquakes included in the catalogue occurred from 1999 to 2020. Solutions were received for 7 or more components, 43% of solutions were received for 9-10 components.

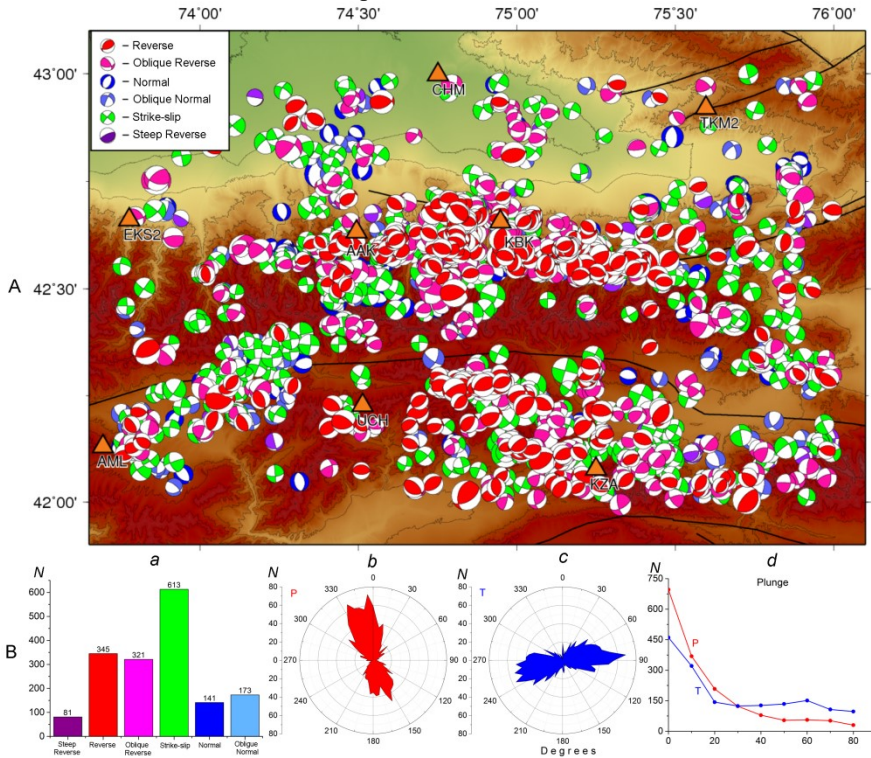


Fig. 4. A – epicentral position and focal mechanisms of earthquake centers (1674). Δ - Stations of the KNET network. B: a - ratio of the number of earthquakes by type of movement; b- diagrams of distribution of compression axes; c - axis of tension; d - the angles of immersion of these axes.

To build a map of focal mechanisms with a designation of the type of movement by color, samples were formed based on the analysis of the plunge angles of the main stress axes (plunge) P_{pl} and T_{pl} . The sampling criterion and quantitative results are presented in table 1.

Table 1. Criteria for choosing the type of mechanism, the number of earthquakes according to the criterion for choosing the type of mechanism for the entire catalogue and for individual depths

| Options | Mechanism types | | | | | | | | | | | |
|---------------------|--|-----|--|------|--|------|---|------|---|------|--|------|
| | A | | B | | C | | D | | E | | F | |
| Selection criterion | $P_{pl} < 30^\circ$ $T_{pl} > 60^\circ$ | | $P_{pl} < 30^\circ$ $T_{pl} > 60^\circ$ | | $P_{pl} < 30^\circ$ $T_{pl} < 30^\circ$ | | $P_{pl} < 30^\circ$ $30 \leq T_{pl} \leq 60$ | | $30 \leq P_{pl} \leq 60$ $T_{pl} < 30^\circ$ | | $30 \leq P_{pl} \leq 60$ $30 \leq T_{pl} \leq 60$ | |
| Quantity | <i>N</i> | % | <i>N</i> | % | <i>N</i> | % | <i>N</i> | % | <i>N</i> | % | <i>N</i> | % |
| All events | 345 | 21 | 141 | 8.4 | 613 | 36.6 | 321 | 19.1 | 173 | 10.3 | 81 | 4.8 |
| $H = 0-5$ km | 8 | 9.4 | 12 | 14.1 | 24 | 28.2 | 15 | 17.6 | 16 | 18.8 | 10 | 11.7 |

| | | | | | | | | | | | | |
|--------------|-----|------|----|------|-----|------|-----|------|----|------|----|-----|
| H = 5-10 km | 95 | 16.6 | 84 | 14.7 | 203 | 35.6 | 89 | 15.6 | 70 | 12.2 | 29 | 5.1 |
| H = 10-15 km | 129 | 23.6 | 25 | 4.5 | 204 | 37.3 | 120 | 21.9 | 46 | 8.4 | 22 | 4 |
| H > 15 km | 113 | 23.8 | 20 | 4.2 | 182 | 38.4 | 97 | 20.5 | 41 | 8.6 | 20 | 4.2 |

Note. A – Reverse fault; B – Normal fault; C – horizontal Strike-slip fault; D – Oblique reverse fault; E – oblique normal fault; F – Steep reverse fault.

In fig. 4A shows the position of the stations of the KNET network and earthquakes with an indication of the type of mechanism (see the inset in Fig. 3A). A variety of focal mechanisms is noted – reverse fault, normal fault, horizontal strike-slip faults, oblique reverse fault and oblique normal fault. A separate part of the events was attributed to steep reverse fault. 40% of events are reverse fault and oblique reverse fault, 41% are horizontal strike-slip faults and steep reverse fault. Normal fault and oblique normal fault are few in number and total 18% (Fig. 4Ba, Table 1.).

The statistical characteristics of the parameters of the axes of the principal stresses make it possible to determine some patterns of deformation processes. Diagrams of the distribution of the azimuths of the compression and extension axes, as well as the diagrams of the dependence of the number of earthquakes on the angle of immersion of these axes, have been constructed. When constructing, the values of the strike angles were averaged with a step of 5 degrees, and the angles of immersion were averaged with a step of 10 degrees.

According to the results obtained, the direction of the compression axes changes from north-north-west to north-north-east (the scatter is limited to the 330° –10° sector) (Fig. 4Bb). For extension axes, the direction of the axes changes from northeast to southeast (the scatter is limited to a sector of 60° –110°) (Fig. 4Bc). This is in good agreement with previously published results [24-26]. The sub-horizontal position (up to 30°) has 75% of the compression axes and 53% of the tension axes (Fig. 4Bd).

Reverse fault and normal fault. In fig. 5A separately presents the distribution of reverse fault earthquakes (345 events, red) and normal fault type (141 events, blue). A joint map of reverse fault and normal fault events makes it possible to assess the ratio of their positions in the study area. The reverse fault seismic events are concentrated in three sublatitudinal zones: in the southern part of the Chuya depression up to its junction with the Chu-Ili mountains, along the northern slope of the central and eastern part of the Kyrgyz ridge and south of the Kyrgyz ridge from the Suusamyr to Kochkor depression through the Sandyk, Karamoinok and Kyzart mountains. The normal fault events are mostly isolated, and their concentration is observed only in the central part of the Kyrgyz ridge at the meridian level of 74.5° E; several events are located in the area of the Suusamyr and Chuya depressions and along the northern slope of the eastern part of the Kyrgyz ridge to the Chu-Ili Mountains. Numerically, normal fault events predominate in the western part of the territory under consideration. The area of normal fault events concentration south of the AAK station and in the south-eastern part of the Chui Depression. In the first case, the zone of reverse fault and normal fault events overlap, in the second they are allocated to a separate area.

In fig. 5B shows diagrams of the *P*- and *T*-axes directions for the reverse fault and normal fault mechanisms. *P*-axes for reverse fault events have three directions: north-north-west, north and north-north-east, *T*-axes are mostly oriented sublatitudinally. The *P*-axes for normal fault mechanisms have many directions, the most representative is the northeast direction, and for the *T*-axes the western direction is the most representative.

It is noted in [27] that, having different rheological properties, the layers of the earth's crust of the Tien Shan react differently to the tectonic compression they experience. According to the study of the azimuths of the compression axes at all considered depths (see Table 1) changes in the 330° – 10° sector, however, the maximum peak value of the number of events with depth shifts from 330° (northwest direction) to 360° (north). The direction of the extension axes for all depths varies from northeast to southeast.

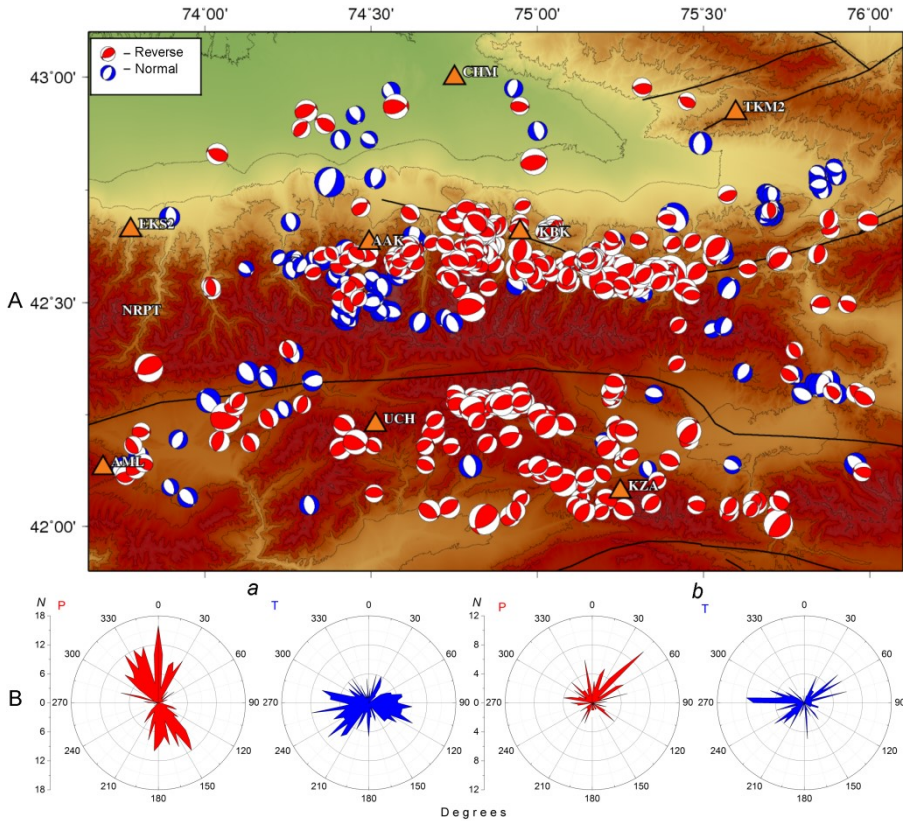


Fig. 5. A - the earthquakes position of the reverse fault and normal fault types. Δ - KNET stations. B - diagrams of the distribution of the azimuths of the compression (P) and tension (T) axes for the mechanisms of reverse fault events (a , 345 events) and normal fault events (b , 141 events).

Dynamic parameters. The dynamic parameters for 183 earthquakes of the Northern Tien Shan have been determined. When calculating the scalar seismic moment M_0 , source radius r , stress drop $\Delta\sigma$, emitted seismic energy E_S and reduced seismic energy e_{PR} according to formulas (2) - (6), the values of the rock density in the source and the shear wave velocities were taken to be equal, respectively, $\rho = 2.6 \text{ g / cm}^3$ [28], $V_S = 3.5 \text{ km/s}$ [29]. The boundary values of the obtained DP values are presented in table. 2. In the further, the DP of 182 earthquakes will be considered. The earthquake of December 25, 2006 with $K = 14.7$, $M_0 \sim 2 \cdot 10^{17} \text{ N}\cdot\text{m}$ and $\Delta\sigma \sim 214 \text{ MPa}$ (which radically differs in value from other events) is excluded from the analysis.

Table 2. Boundary values of dynamic parameters (182 earthquakes).

| Parameters | K | M | $f_0, \text{ Hz}$ | $M_0, \text{ N}\cdot\text{m}$ | $r, \text{ m}$ | $\Delta\sigma, \text{ MPa}$ | $E_S, \text{ J}$ | e_{PR} |
|------------|------|-----|-------------------|-------------------------------|----------------|-----------------------------|----------------------|----------------------|
| Min | 8.7 | 2.6 | 1.7 | $6.2 \cdot 10^{12}$ | 210 | 0.2 | $1.08 \cdot 10^7$ | $1.75 \cdot 10^{-6}$ |
| Max | 13.7 | 5.4 | 6.0 | $2.7 \cdot 10^{16}$ | 690 | 42 | $8.03 \cdot 10^{12}$ | $0.33 \cdot 10^{-3}$ |

The dependences of the dynamic parameters on the scalar seismic moment, the magnitude M , recalculated from the class K , were constructed, and the correlation coefficients between the DP and the magnitude, between the DP and the scalar seismic moment were calculated. Table 3 the obtained correlation coefficients are presented, as well as some regression dependences. The largest correlation coefficient between the seismic

moment M_0 and the seismic energy E_S ($k = 0.98$), the smallest between the seismic moment M_0 and the stress drop $\Delta\sigma$ ($k = 0.74$). Let us consider the features of the distributions of the parameters of the spectral characteristics Ω_0, f_0 and the dynamic parameters for 182 events.

Table 3. Regression dependences and correlation coefficients of dynamic parameters of earthquake sources and their magnitude and seismic moment.

| № | Parameter | Parameter | Correlation coefficient, k | Model |
|---|----------------|-----------|------------------------------|--|
| 1 | $\lg \Omega_0$ | M | 0.88 | $\lg \Omega_0 = 1.12M - 8.27$ |
| 2 | $\lg e_{PR}$ | M | 0.78 | $\lg e_{PR} = 0.63 \cdot M - 7.1$ |
| 3 | $\lg M_0$ | M | 0.88 | $\lg M_0 = 1.10M + 10.1$ |
| 4 | e_{PR} | M_0 | 0.74 | $e_{PR} = 7 \cdot 10^{-14} \cdot M_0^{0.59}$ |
| 5 | $\Delta\sigma$ | M_0 | 0.74 | $\Delta\sigma = 6.1 \cdot 10^{-7} \cdot M_0^{0.47}$ |
| 5 | $\Delta\sigma$ | $\lg M_0$ | 0.78 | $\Delta\sigma = 2.3 \cdot 10^{-19} \cdot \lg M_0^{16}$ |
| 6 | f_0 | $\lg M_0$ | -0.85 | $f_0 = 21 - 1.16 \cdot \lg M_0$ |
| 7 | $\lg E_S$ | $\lg M_0$ | 0.98 | $\lg E_S = 1.59 \cdot \lg M_0 - 13.18$ |
| 8 | $\lg e_{PR}$ | $\lg M_0$ | 0.92 | $\lg e_{PR} = 0.59 \cdot \lg M_0 - 13.15$ |
| 9 | r | $\lg M_0$ | 0.84 | $r = 116 \cdot \lg M_0 - 1327$ |

Spectral density and scalar seismic moment. The distribution of the parameter Ω_0 (on a logarithmic scale) depending on the magnitude is shown in Fig. 6a, and the distribution of the scalar seismic moment for the same events ($M_0 \sim \Omega_0$) is shown in Fig. 6b. These logarithmic distributions are well described by the line model. For a scalar seismic moment, the regression dependence on magnitude (best model) can be written in the form:

$$\lg M_0 = 1.1M + 10.1 \tag{7}$$

The correlation coefficient between the values of $\lg M_0$ and the magnitudes M is 0.88. The deviation of the values relative to the linear model (regression lines in Fig. 6b) is uniform over the entire range of the considered values.

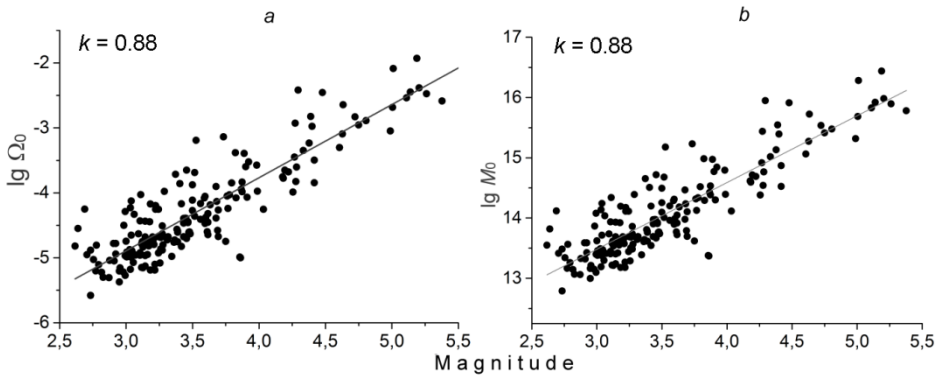


Fig. 6. Logarithmic distributions of spectral density (a) and scalar seismic moment (b) versus magnitude. k is the correlation coefficient.

For the events under consideration, the range of magnitude variation is $2.2 \leq M \leq 6.0$, and the values of M_0 lie in the range from $6.2 \cdot 10^{12}$ to $2.2 \cdot 10^{17}$ N·m. It should be noted that, due to the presence of a scatter and a relatively narrow range of magnitudes, the distribution of $\lg M_0$ also agrees (with an accuracy of 10%) with the well-known expression $\lg M_0 = 1.6M + 8.4$ [16].

Taking into account the high value of the correlation coefficient between the magnitudes and the values of the logarithm of the seismic moment, in the future, in a number of cases, we will consider the distribution of DP depending on $\lg M_0$

Corner frequency and source radius. In fig. 7a shows the distribution of f_0 as a function of $\lg M_0$. The corner frequency is characterized by a decrease with increasing $\lg M_0$ or magnitude. The source radius was determined from the values of the corner frequency using formula (2). The distribution of r values depending on the logarithm of the seismic moment is shown in Fig. 7b. The Brune radius r varies from approximately 210 to 640 m.

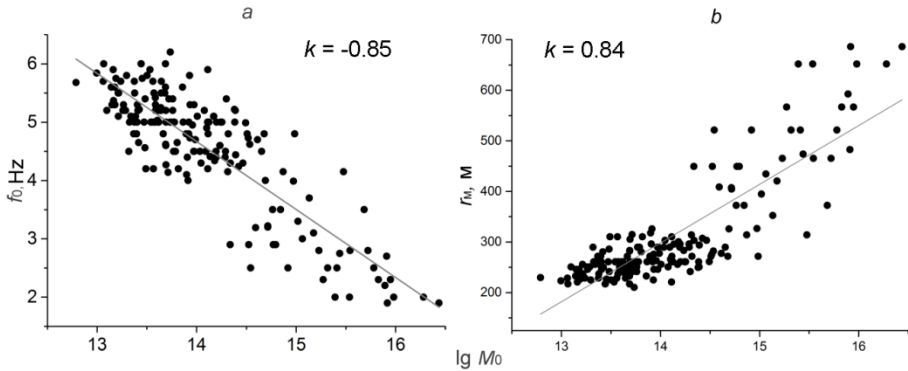


Fig. 7. The values of the corner frequency (a) and the source radius (b) in comparison with $\lg M_0$.

Distribution of sources radius in Fig. 7b allows linear approximation in terms of $\lg M_0$: $\lg M_0: r = 116 \cdot \lg M_0 - 1327$. The deviations of r values from the linear model for events with $\lg M_0 < 14.5$ turned out to be smaller than for events with $\lg M_0 > 14.5$. The correlation coefficient between the r and $\lg M_0$ values is about 0.84.

Seismic energy and reduced seismic energy. The logarithmic distribution of the seismic energy E_S and the reduced seismic energy e_{PR} in comparison with the values of $\lg M_0$ is shown in Fig. 8. Seismic energy varies in the range from $\sim 1.0 \cdot 10^7$ to $\sim 8.0 \cdot 10^{12}$ J (see Table 2).

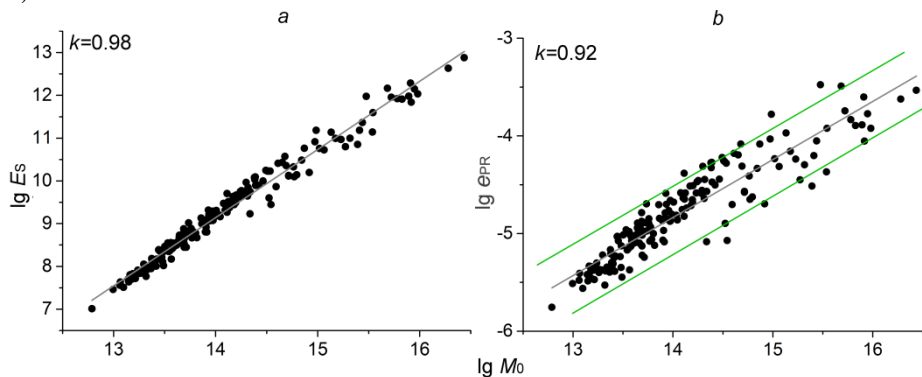


Fig. 8. Distribution of seismic (a) and reduced seismic energy (b) versus seismic moment on a double logarithmic scale.

The linear model describing the E_S distribution has the form $\lg E_S = 1.6 \cdot \lg M_0 - 13.2$, and the correlation coefficient between seismic energy and scalar moment is $k = 0.98$. For the events under consideration, the e_{PR} parameter is on the order of $1.8 \cdot 10^{-6}$ to $\sim 0.3 \cdot 10^{-3}$ (see Table 2). The distribution of $\lg e_{PR}$ is also described by a linear model, although for it the

scatter of values relative to the regression line is greater in comparison with the case in Fig. 8a. The expression for the linear model (regression dependence) has the form

$$\lg e_{PR} = 0.6 \cdot \lg M_0 - 13, M_0 (\text{N}\cdot\text{m}), \quad (8)$$

moreover, the correlation coefficient between the values of $\lg e_{PR}$ and the logarithm of the scalar seismic moment is 0.92.

Fig. 8b shows that the e_{PR} values are localized in a strip, the boundaries of which are parallel to the approximating straight line: about 95% of the imaging points fall inside such strips. The boundaries of the localization band of the $\lg e_{PR}$ values in Fig. 8b are determined by the ratio: $0.59 \cdot \lg M_0 - 13.6 \leq \lg e_{PR} \leq 0.59 \cdot \lg M_0 - 12.9$.

Stress drop. The values of the stress drop are in the range from 0.2 to ~ 40 MPa (Table 2). There is only one earthquake on 25.12.2006, $M = 6$ with $\Delta\sigma \approx 214$, which is excluded from the analysis. The distribution of the stress drop together with the values of $\lg M_0$ is shown in Fig. 9a. The best approximation of the $\Delta\sigma$ distribution is a power-law dependence on $\lg M_0$. Let us explain this circumstance. According to expressions (6), (4), (2), the values of the dropped stresses and reduced seismic energy are proportional: $\Delta\sigma \sim e_{PR}$. Consequently, the distribution $\lg \Delta\sigma$ will differ from that shown in Fig. 8b of the logarithmic distribution of e_{PR} only by a vertical shift by some constant. For the calculation results for $\Delta\sigma$, the following approximation is obtained: $\Delta\sigma = 3.0 \cdot 10^{-8} \cdot M_0^{0.59}$. The correlation coefficient between drop stress and seismic moment is $k = 0.74$ (Table 3).

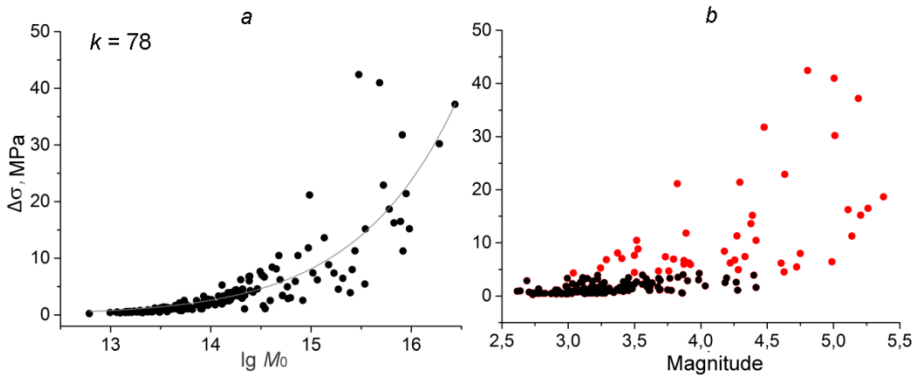


Fig. 9. Distribution of dropped stresses in comparison with the values of $\lg M_0$ (a) and the result of clustering (b) of the representing points on the graph $\Delta\sigma(M)$.

Fig. 9a, it can be seen that the scatter of $\Delta\sigma$ values relative to the regression line increases for events with $\lg M_0 > 14.5$ (magnitudes $M > 4.0$). Taking this into account, the issue of correlations between $\Delta\sigma$ and $\lg M_0$ was analyzed in more detail, for which several samples of events were formed (Table 4), and for each of them the correlation coefficients were determined. The first two samples were made according to the values of $\lg M_0$, which characterizes the scale of earthquakes: events with $\lg M_0 < 14.5$ constituted the first sample, and events with $\lg M_0 \geq 14.5$ - the second. Two more samples were formed on the basis of stress drop: the third sample included events with $\Delta\sigma < 10$ MPa, and the fourth - $\Delta\sigma \geq 10$ MPa. The distinction based on the $\Delta\sigma$ feature corresponds with good accuracy to the selection of two clusters in the distribution of significant points in Fig. 9b using the clustering algorithm [30-31]. The distribution of stress drop for the first two samples is shown in Fig. 10a, the latter in Fig. 10b. The color of the icons indicates that the events belong to one of the selections.

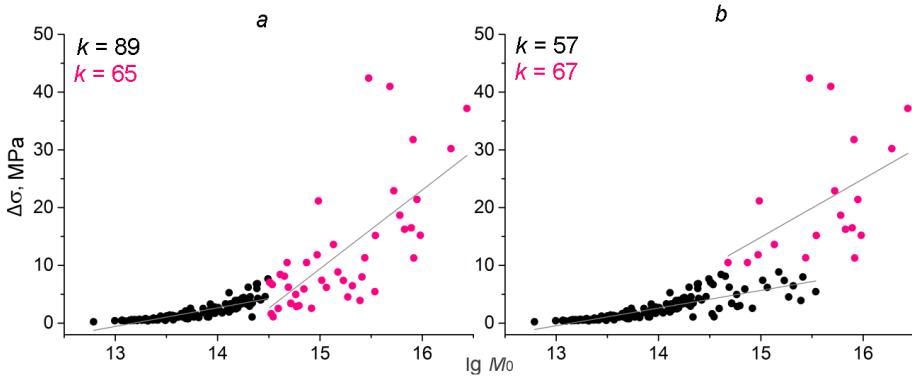


Fig. 10. Distribution of stress drop depending on the logarithm of the scalar moment: a - for events with $\lg M_0 < 14.5$ - black color, $\lg M_0 \geq 14.5$ - crimson color; b - for events with $\Delta\sigma < 10$ - black color, for $\Delta\sigma \geq 10$ MPa - crimson.

Table 4. Regression dependences and correlation coefficients of dynamic parameters of earthquake sources and their magnitude and seismic moment.

| № | Sample for $\Delta\sigma$ | Parameter | Correlation coefficient, k | Model |
|----------|---|------------------|--|---|
| 1 | Bce $\Delta\sigma$ | M_0 | 0.78 | $\Delta\sigma = 3 \cdot 10^{-8} \cdot M_0^{0.59}$ |
| 2 | $\lg M_0 < 14.5$ | M_0 | 0.89 | $\Delta\sigma = 4 \cdot 10^{-11} \cdot M_0^{0.8}$ |
| 3 | $\lg M_0 \geq 14.5$ | M_0 | 0.65 | $\Delta\sigma = 6 \cdot 10^{-7} \cdot M_0^{0.50}$ |
| 4 | $\Delta\sigma < 10$ MPa | M_0 | 0.57 | $\Delta\sigma = 4 \cdot 10^{-8} \cdot M_0^{0.58}$ |
| 5 | $\Delta\sigma \geq 10$ MPa | M_0 | 0.67 | $\Delta\sigma = 8 \cdot 10^{-5} \cdot M_0^{0.37}$ |

Table 4 shows the values of the correlation coefficients between the stress drop and the logarithm of the seismic moment for the above-described samples, as well as for the general sample of 182 events. For samples with $\lg M_0 \geq 14.5$ and with $\Delta\sigma \geq 10$, the correlation coefficients are lower than for the general sample and there is a significant scatter of values relative to the regression line. The high value of the correlation coefficient for events with $\lg M_0 < 14.5$ is reflected in the graph by the fact that the points of the values of $\Delta\sigma$ in Fig. 10a are more localized near the regression line than points for another sample of events (crimson). For $\Delta\sigma < 10$ MPa, the correlation coefficient is low, which is explained by a small change in the values of the stress drop for the considered sample of events (black dots in Fig.10b). Such formal correlations convey physical meaning to a lesser extent than the correlations between the stress drop and M_0 , or between the logarithms of these quantities. The obtained regression dependences, in which the exponent of M_0 is not less than 0.37, as well as Fig. 10 indicate the absence of self-similarity of earthquake sources on the territory of the BGGP in terms of stress drop and reduced seismic energy ($\Delta\sigma \sim e_{PR}$).

Conclusion

For weak earthquakes that occurred on the territory bounded by the coordinates of the edge stations of the KNET network (completely surrounded by stations), the focal mechanisms of the sources were determined by the signs of the arrival of P -waves and a catalogue of focal mechanisms was formed, which includes 1674 earthquakes that occurred from 1994 to 2020 biennium. In the region under consideration, mainly three groups of sources are formed, differing in the nature of the movements occurring in them: reverse fault, oblique reverse fault, and horizontal strike-slip faults. The Normal fault and oblique

normal fault events occur less frequently and are localized to a greater extent. A significant part of the events are reverse fault and oblique reverse fault events, most of which have a near-horizontal compression axis. For weak events, the prevailing direction of the azimuths of the compression axes is north-north-west (with depth this direction changes from north-north-west to north), and for extension axes - east-north-east.

A data bank has been formed on the dynamic parameters of earthquakes that occurred on the territory of the Northern Tien Shan (BGPG) in 1998–2017 (183 events). Distributions of dynamic parameters from magnitude M and scalar seismic moment M_0 are constructed, regression equations and correlation coefficients of dynamic parameters and scalar seismic moment are obtained. For a scalar seismic moment, the regression dependence on magnitude has the form: $\lg M_0 = 1.1M + 10.1$ for BGPG, which is in good agreement with the well-known relationship given by Yu.V. Riznichenko. For earthquake sources on the territory of BGPG, regression was established - a power-law dependence of stress drop on the scalar seismic moment with a correlation coefficient of 0.74. The main contribution to the correlation is made by seismic events with $M_0 < 3 \cdot 10^{14}$ N·m ($\lg M_0 < 14.5$). For stronger earthquakes with $\lg M_0 \geq 14.5$, the correlation coefficient between the values of $\Delta\sigma$ and M_0 is no more than 2/3, and this makes it possible to understand the results of works in which no significant correlations were found between the stress drop and the seismic moment (they did not consider relatively weak developments). The presence of an increasing dependence of the stress drop and reduced seismic energy on the seismic moment, established for the BGPG, is consistent with the results on the power-law dependence of $e_{PR}(M_0)$ in a number of other regions. The get data on focal mechanisms and dynamic parameters can be used to assess the stress-strain state.

Acknowledgements

The research was partially carried out within the framework of the state assignment of Research Station of the Russian Academy of Sciences in Bishkek city (thems № AAAA-A19-119020190064-9 and № AAAA-A19-119020190066-3).

References

1. N.A. Sycheva, A.N. Mansurov, I.V. Sychev, S.I. Kuzikov, *Vulkanologiya I Sesmologiya*, **3** (2020) (in Russian)
2. N.A. Sycheva, A.N. Mansurov, *Geophysical Research*, **19**, (2018)
3. N.A. Sycheva Dis. ... Cand. physical-mat. Sciences (Moscow) (2005)
4. V.G. Trifonov, O.V. Soboleva, R.V. Trifonov, G.A. Vostrikov *Modern geodynamics of the Alpine-Himalayan collision belt* (GEOS, Moscow, 2002)
5. A.A. Lukk, V.I. Shevchenko, V.G. Leonova, *Physics of the Solid Earth*, **51**, 6 (2015).
6. A.A. Lukk, V.I. Shevchenko *Seismicity Izvestiya Physics of the Solid Earth*, **55**, 4 (2019)
7. A.V. Vvedenskaya, *Study of stresses and ruptures in earthquake sources using the theory of dislocations* (Nauka, Moscow, 1969) (in Russian)
8. J.A. Snoke, J.W. Munsey, A.C. Teague, G.A. Bollinger, *Earthquake Notes*, **55**, 3 (1984)
9. J.A. Snoke, *Earthquake Mechanisms*, *Encyclopedia of Geophysics* (Van Nostrand Reinhold Company, 1989)
10. J.A. Snoke, *Seismological Research Letters*, **61** (1990)
11. J.A. Snoke, *FOCMEC FOCal MECHANism determinations. A manual* (2000)

12. P.A. Reasenberg, D. Oppenheimer, FPFIT, FPLOT and FPPAGE: FORTRAN Computer Programs for Calculating and Displaying Earthquake Fault-Plane Solutions (US Geological Survey Open-File Report, 1985)
13. N.A. Sycheva, L.M. Bogomolov, *Russian Geology and Geophysics*, **57**, 11 (2016)
14. N.A. Sycheva, L.M. Bogomolov, S.I. Kuzikov, Computational technologies in seismological research (on the example of KNET, Northern Tian Shan). (Yuzhno-Sakhalinsk: IMGG FEB RAS, 2020)
15. K. Aki, P. Richards, *Quantitative seismology. Theory and methods* (Mir, Moscow, 1983)
16. Yu.V. Riznichenko, *Problems of seismology* (Nauka, Moscow, 1985)
17. C.H. Scholz *The mechanics of earthquakes and faulting* (Cambridge Univ. Press, Cambridge, 2019)
18. R.E. Abercrombie, J.R. Rice, *Geophysical Journal International*, **162** (2005)
19. M.M. Scuderi, C. Marone, E. Tinti, G. Di Stefano, C. Collettini, *Nature Geoscience*, **9**, 9 (2016)
20. S.J. Gibowicz, A. Kijko, *An introduction to mining seismology*. (Academic Press, San Diego, 1994)
21. J.D. Eshelby, *Proceedings of the Royal Society of London* **A241**, 1226, (1957)
22. J. Boatwright, *Bulletin of the Seismological Society of America*, **70** (1980)
23. R. Madariaga, *Earthquake scaling laws* In: R.A. Meyers, ed. *Extreme environmental events: Complexity in forecasting and early warning* (Springer, 2011)
24. V.N. Krestnikov, E.I. Shishkin, D.V. Shtange, S.L. Yunga, *Izvestiya Academy of Sciences of the USSR Physics of the Earth*, **3** (1987) (in Russian)
25. S.L. Yunga, *Methods and results of studies of seismotectonic deformations* (Nauka, Moscow, 1990)
26. A.K. Kurskeev, *Earthquakes and seismic safety of Kazakhstan* (Evero, Almaty, 2004)
27. F.N. Yudakhin, T.Ya. Belenovich, *Izvestiya Academy of Sciences Kirg. SSR Fiz Tech. and matem. Science*, **1** (1989)
28. D.K Chedia, *Morphostructures and the latest tectogenesis of Tian Shan* (Ilim, Frunze, 1986)
29. S.W. Roecker, T.M. Sabitova, L.P. Vinnik., Y.A. Burmakov, V.I. Golvanov, R. Mamatkanova., L. Munirova, *Journal Geophysical Research*, **98** B9 (1993)
30. R.F. Ling, *The Computer Journal*, **15**, 4 (1972)
31. J. Sander, M. Ester, H. Kriegel, X. Xu *Data, Mining and Knowledge Discovery*, **2**, 2 (1998)